LAWRENCE
LIVERMORE
NATIONAL
LABORATORY

LLNL-JRNL-485617

Internal 26Al-26Mg isotope systematics of a type B CAI: Remelting of refractory precursor solids

N. T. Kita, T. Ushikubo, K. B. Knight, R. A. Mendybaev, A. M. Davis, F. M. Richter, J. Fournelle

June 6, 2011

Geochimica et Cosmochimica Acta

Disclaimer

Internal ^{26}Al-^{26}Mg isotope systematics of a Type B CAI: Remelting of refractory precursor solids

Noriko T. Kita[1*], Takayuki Ushikubo[1], Kim B. Knight[2,3,5], Ruslan A. Mendybaev[2,3], Andrew M. Davis[2,3,4], Frank M. Richter[2,3], and John Fournelle[1]

[1]WiscSIMS, Department of Geoscience, University of Wisconsin-Madison, 1215 W. Dayton St., Madison WI 53706.

[2]Chicago Center for Cosmochemistry

[3]Department of the Geophysical Sciences, The University of Chicago, Chicago, IL 60637

[4]Enrico Fermi Institute, The University of Chicago, Chicago, IL 60637

To be submitted to Geochim. Cosmochim. Acta

January X, 2011

[*]*Corresponding author (noriko@geology.wisc.edu)*

[5]*Present address: Lawrence Livermore National Laboratory, Livermore, CA 94550.*

Abstract:

The high precision SIMS ^{26}Al-^{26}Mg isotope analyses of a pristine type B1 CAI in Leoville 3535-1 are obtained from multiple mineral phases that include Al-rich zoned melilite mantle, Mg-rich melilite, fassaite, spinel and anorthite in the core. The data yield a well-defined internal isochron with the inferred initial ^{26}Al/^{27}Al ratio of $(5.002\pm0.065)\times10^{-5}$ and the intercept of δ^{26}Mg* = 0.06±0.08 ‰. Assuming homogeneous distribution of ^{26}Al in the solar system, Leoville 3535-1 formed 46±29 ky after the time of bulk CAI isochron. One anorthite analysis near the grain boundary adjacent to melilite shows sub-μm scale heterogeneous Mg distribution, though the ^{26}Al-^{26}Mg data plot exactly on the same isochron regression line with other data. Thus, the internal ^{26}Al-^{26}Mg system of the CAI was remained closed since the last melting events that crystallized anorthite.

High precision Mg isotope analyses of Mg-rich minerals (fassaite, Mg-rich melilite, and spinel) show a small scatter from the regression line (~0.1‰) beyond analytical uncertainties. Spinel and fassaite data systematically displaced below and above the regression line, respectively, which might be caused by incomplete isotope resetting during last melting event. The following scenario may explain the observed ^{26}Al-^{26}Mg system among different mineral phases. The Leoville 3535-1 CAI with zoned melilite mantle initially formed from nearly complete melting of refractory precursors immediately after the time of bulk CAI isochron. Later reheating event of the CAI that postdated ~50ky, resulted in partial melting, in which fassaite and anorthite crystallized.

The short time scale less than 0.1 Myr inferred from the Leoville type B CAI may corresponds to the active protostar stage (known as “Class 1”), during which high temperature sporadic heating events occurred repeatedly to the refractory solids in the solar nebula.

1. Introduction

Ca, Al-rich inclusions (CAIs) in primitive meteorites consist mainly of Ca and Al-rich minerals that are expected to condense from the gas of solar composition at high temperature (e.g., Grossman, 1972; MacPherson, 2005). They are the oldest objects in the solar system ever measured by the U-Pb absolute chronometer (Amelin et al., 2002; Connelly, 2008; Bouvier and Wadhwa, 2010) and they have large ^{16}O enrichments ($\delta^{18}O \sim \delta^{17}O \sim -50‰$; Clayton, 1973) relative to earth, moon and most bulk meteorites, that is consistent with the composition of the sun recently estimated from the analysis of solar wind collected by the Genesis space craft (McKeegan et al., 2008). CAIs occur in almost all types of chondritic meteorites and also among particles collected by the Stardust mission from Comet 81P/Wild2 (Zolensky et al., 2006; McKeegan et al., 2006), indicating that CAIs are ubiquitously distributed throughout the early solar system. Shu et al. (1996) suggested CAIs formed close to the young sun, lifted and transported to asteroidal belt by the magnetically driven wind (X-wind model). Other transport mechanisms from inner solar nebula have also been proposed (Cuzzi et al., 2003; Ciesla, 2007).

Lee et al. (1977) first reported clear evidence of in-situ decay of ^{26}Al (half life; 0.73Myr) from the mineral separates of the CAI "WA", showing the correlated excess of ^{26}Mg from the decay of ^{26}Al with $^{27}Al/^{24}Mg$ ratios and inferred initial $^{26}Al/^{27}Al$ ratios of $(5.1\pm0.6)\times10^{-5}$. MacPherson et al. (1995) summarized the literature data available at the time and found that most CAIs consistently show the initial $^{26}Al/^{27}Al$ ratios of $\sim5\times10^{-5}$, which is referred to as "canonical" value. However, a spread of initial $^{26}Al/^{27}Al$ ratios among CAIs was not well defined because of analytical limitation and possible later disturbance of some of the CAIs (e.g., Podosek et al., 1991). Recently, several studies have re-evaluated the initial $^{26}Al/^{27}Al$ ratios of CAI with

68 improved analytical precisions using inductively coupled plasma mass spectrometers (ICP-MS)
69 or secondary ion mass spectrometers (SIMS), which has resulted in a vigorous debate as to the
70 actual value of initial $^{26}Al/^{27}Al$ ratio of CAIs with values as high as $(6\text{-}7)\times10^{-5}$ being proposed.
71 (Bizzarro et al., 2004; 2005; Young et al., 2005; Thrane et al., 2006; Cosarinsky et al., 2007;
72 Jacobsen et al., 2008; Baker 2008; MacPherson et al., 2010a). In particular, both Thrane et al.
73 (2006) and Jacobsen et al. (2008) obtained well-correlated isochrons from multiple whole-rock
74 CAIs in CV3 chondrites, but their inferred initial $^{26}Al/^{27}Al$ ratios are significantly different by
75 11% with reported values of $(5.85\pm0.05)\times10^{-5}$ and $(5.23\pm0.13)\times10^{-5}$, respectively. There could
76 be multiple causes for the discrepancy of the inferred initial $^{26}Al/^{27}Al$ ratio, including the method
77 of data reduction (e.g., Bizzarro et al., 2005; Davis et al., 2005; Jacobsen et al., 2008) and the
78 disturbed ^{26}Al-^{26}Mg values from in-situ techniques such as Laser ICPMS and SIMS (e.g., Young
79 et al., 2005; Cosarinsky et al., 2007; Connolly et al., 2009; 2010). It should be mentioned that
80 many CAIs previously studied might have experienced alteration in their parent bodies, such as
81 thermal metamorphism, aqueous alteration and shock reheating (e.g., Podosek et al., 1991;
82 Nakamura et al., 1992; Caillet et al., 1993; Fagan et al., 2007). Formation of secondary minerals
83 in the CAIs might cause either open or closed system redistribution of Al and Mg, which may
84 explain the disturbed data on the Al-Mg isochron diagram. In such cases, accurate and reliable
85 initial $^{26}Al/^{27}Al$ ratios would not be obtained.

86 In this study, we report high precision SIMS Al-Mg isotope study of a pristine large
87 igneous Type B1 CAI (Leoville 3535-1) that is one of the least altered CAI without any sign of
88 secondary mineralization. The improved analytical precision of the new generation SIMS
89 (IMS-1280 at the University of Wisconsin-Madison; WiscSIMS, Valley and Kita, 2009; Kita et
90 al., 2009) allows us to evaluate the linearity of data in an isochron diagram and to test if the

Al-Mg isotope system in the CAI was remained closed.

2. Analytical Method

2.1. Sample

The sample used in the present study is a large (8mm x 6mm) Type B1 CAI (US National Museum of Natural History designation USMN 3535-1) from the CV3 meteorite Leoville (Fig. 1). The CAI was originally chosen for a study of the internal distribution of Mg and Si isotope fractionations (Richter et al., 2007; Knight et al., 2009). The outer edge of the CAI is surrounded by a thick (500μm) melilite mantle that shows major element zoning with increasing Åk contents from the rim to the interior ($Åk_{20}$-$Åk_{60}$). The texture and zoning indicates that the CAI crystallized inwards from the edge. Minor amount of small spinel grains (<20μm) also occur within mantle melilite. The core consists of Åk-rich melilite ($Åk_{65-80}$), fassaite, anorthite and spinel. TiO_2 contents of fassaite vary up to 10%, generally showing higher TiO_2 in the melilite mantle and lower TiO_2 in the core. There are no secondary minerals, such as nepheline and sodalite, observed in this CAI. SEM-EDX elemental maps of several areas of the CAI have been made and the Al-Mg chronology data reported in this paper are mainly from areas for which elemental maps are available.

The CAI section was originally potted in a 25mm diameter by13mm high polyphenol plug . Because the sample degassed significantly in the SIMS instrument, which would be a problem for Si isotope analyses and the sample height was not compatible with the regular SIMS sample holder (12mm) the sample was later made into a polished thin section with the original surface attached to the slide glass. The new thin section surface is within 40μm of the original

surface, but as the mirror image. The Al-Mg data reported in this paper were obtained from both the original surface and from the thin section.

2.2. Electron Microscopy

In order to guide the location of the SIMS analyses, we obtained detailed and secondary electron (SE) and back scattered electron (BSE) images using a scanning electron microscope Hitachi S-3400 at the University of Wisconsin-Madison. Additional images are obtained after SIMS analyses, in order to examine the analyzed spots for potential inclusions and any other specific features that might have affected the SIMS analyses.

In the early stage of this work, we did not have multiple melilite standards with homogeneous Al and Mg contents that could be used for SIMS $^{27}Al/^{24}Mg$ calibration. Therefore, the major element compositions of melilite in the CAI were obtained using the Cameca SX51 electron microprobe analyzer (EPMA) at the University of Wisconsin with an accelerating voltage of 15kV and a focused beam of 12nA. Pure synthetic åkermanite and gehlenite crystals (provided by professor Morioka of the Radioisotoe Center at the University of Tokyo), which had been made as described in Marioka and Nagasawa (1991), were used as EPMA calibration standards. We also obtained major element compositions of fassaite at the location of the SIMS analyses using EPMA.

2.3. SIMS Al-Mg isotope analyses

The CAMECA IMS-1280 at the University of Wisconsin-Madison (WiscSIMS, Valley and Kita, 2009; Kita et al., 2009) was used for the SIMS Al-Mg isotope analyses. We used O^- primary ions with total impact energy of 23kV (-13kV at the ion source and +10kV at the sample

surface) and detected Mg^+ and Al^+ secondary ions. We used two different analytical conditions for anorthite and other Mg-rich minerals (melilite, fassaite and spinel), mono-collection electron multiplier (mono-EM) and multi-collection Faraday cups (MC-FC), respectively, due to the difference in secondary Mg intensities. The CAI analyses were made in three sessions; analyses of melilite mantle on MC-FC mode (S1), analyses of anorthite on mono-EM mode (S2), and analyses of three Mg-rich minerals melilite, fassaite, and spinel in both mantle and core the CAI on MC-FC mode (S3).

2.3.1. Multi-collection FC analysis (S1 and S3)

For multi-collection FC analyses, the primary O^- ion beam was adjusted to produce a 20μm×25μm oval shape with the intensity of 7nA (spinel) and 20nA (melilite and fassaite). By using the Duo lens (new primary ion lens between Duoplasmatron ion source and primary beam mass filter), a primary ion intensity of 20nA is easily obtained in Koehler illumination mode with mass and beam apertures of 200 μm and 750 μm diameters, respectively, where the mass aperture determines the size of primary beam. In this condition, SIMS analysis pits show a small amount of aberration and the carbon coat is removed for ~40μm areas, though direct secondary ion images show that the majority of secondary ions are created only from a central 20-25μm area. For spinel analyses with higher Mg contents, we inserted 400μm beam aperture in order to remove the aberration of the primary beam. This condition made aiming of analysis location much easier for spinel with grain sizes typically smaller than 20μm, though the primary beam intensity was reduced to 7nA. Examples of SIMS pits produced by the different analysis conditions are shown in Fig. 2.

Secondary ion optics were adjusted to ×200 magnification from sample to the Field

Aperture (FA, 6000µm square) with mass resolving power of ~2,500 (entrance slit; 90µm and exit slit 500µm), which was enough to separate both $^{48}Ca^{++}$ and MgH^{+} interferences from the Mg mass spectrum. The energy slit was set to 40eV. Four multi-collection FC detectors were used to detect $^{24}Mg^{+}$, $^{25}Mg^{+}$, $^{26}Mg^{+}$ (with 10^{11} ohm resistors) and $^{27}Al^{+}$ (with 10^{10} ohm resistor) simultaneously, with ^{25}Mg set to the ion optical axis. Due to the primary beam size transferred to the FA [give full name of FA]plane is comparable to the size of the FA, we applied XY-mode {explain] by using rectanglar lenses at the coupling optics (between an electrostatic analyzer and a sector magnet) to reduce aberration of the mass spectrum. In general, XY-mode would cause Y-deflection of the secondary beam but we did not find a significant difference in Y-deflection among four detectors. Secondary $^{24}Mg^{+}$ and $^{27}Al^{+}$ ions intensities were (0.5-3) $\times 10^{8}$ cps and (1-4) $\times 10^{8}$, respectively, depending on the mineral phase. A single analysis takes 8 min, including 60s of presputtering, ~120s for automated centering of the secondary optics, and 300s of integration (10s ×30 cycles) of the Mg and Al signals. The baseline of the FC detectors was monitored during presputtering and averaged over 8 analyses. Due to difference in Mg secondary intensities, we run each mineral separately. The melilite glass standard (~$Åk_{65}$), fassaite glass standard with 5 wt.% TiO_2 and natural spinel standard were used as running standard for melilite, fassaite and spinel analysis, respectively. In addition, multiple synthetic and natural standards were used to evaluate analytical conditions (Table EA1 in electronic annex1). Comprehensive descriptions of these standards will be reported elsewhere. A total of 8 sets of standard analyses were obtained by bracketing 8-10 unknown sample analyses and the average of the 8 standard analyses were used to correct for instrumental bias on the measured Mg isotope ratios. The measured ratios ($^{25}Mg/^{24}Mg$ and $^{26}Mg/^{24}Mg$) are converted to δ-notations ($\delta^{25}Mg$ and $\delta^{26}Mg$) by normalizing to the terrestrial reference ratios of ($^{25}Mg/^{24}Mg$)= 0.12663 and ($^{26}Mg/^{24}Mg$)=

183 0.13932 (Catanzaro et al., 1966), respectively.

184 An isotope mass fractionation correction (both instrumental and natural) is applied to the
185 SIMS measured Mg isotope ratios in order to estimate excess ^{26}Mg. The fractionation-corrected
186 δ^{26}Mg* values were calculated using an exponential law with coefficient β= 0.514 from the
187 evaporation experiment of Davis et al. (2011).

188

189 $$\delta^{26}\mathrm{Mg}^* = \delta^{26}\mathrm{Mg} - \left(1 + \delta^{25}\mathrm{Mg}/1000\right)^{-\beta} \quad (1)$$

190

191 Both the internal errors and the reproducibility of fractionation-corrected δ^{26}Mg* values for
192 standards were typically 0.03-0.05‰ (2SD) for a fassaite glass (FAS-G H5; TiO_2=4.8%) and
193 spinel standards and 0.05-0.09‰ (2SD) for the $Åk_{65}$ glass standard. We always see a slight offset
194 of δ^{26}Mg* values at the level of 0.1-0.3‰ between glass and mineral standards, which we
195 attribute to a small instrumental bias, possibly due to the efficiency of the detectors or some
196 other unknown matrix effects. The offset is corrected according to the value obtained from the
197 bracketing standard analyses. For Al-rich melilite glass standards ($Åk_{15-25}$), reproducibility of
198 standard was degraded to 0.15-0.20‰ due to lower Mg ion intensities, though they are
199 comparable to the internal errors of individual analyses. For fassaite glass standards, the δ^{26}Mg*
200 values in 2 standards with TiO_2=1.9% are systematically lower by nearly 0.1‰, so that we
201 applied the second order correction linearly with TiO_2 contents and included an additional
202 0.05‰ uncertainty that propagated to the final error. The second order correction for Ti in the
203 CAI fassaite (2.5%-8.6% TiO_2) are less than 0.07‰ (see electronic annex2).

204 The instrumental biases on δ^{25}Mg in melilite and fassaite were estimated from the
205 analyses of multiple standards, which for melilite increases by 1‰ linearly from $Åk_{15}$ and $Åk_{100}$

and decrease by 0.6‰ in fassaite from TiO_2=2% to 10% (EA2). The $\delta^{25}Mg$ values in the CAI minerals were corrected according to their Åk molar % and TiO_2 wt% for melilite and fassaite, respectively. The instrumental bias on $\delta^{25}Mg$ in spinel is estimated by assuming the $\delta^{25}Mg$ value in the standard to be 0. Because the standard is very close to pure $MgAl_2O_4$ (0.6% FeO), we corrected matrix effects on $\delta^{25}Mg$ measurements of spinel in CAIs using data from our spinel standard.

The reproducibility of the measured $^{27}Al/^{24}Mg$ ratios of the standards was better than 1% (2SD). Relative sensitivity factors (RSF) of $^{27}Al/^{24}Mg$ ratios were calculated by comparing those of raw SIMS data and those calculated from EPMA analyses.

$$RSF = (^{27}Al/^{24}Mg)_{SIMS}/(^{27}Al/^{24}Mg)_{EPMA} \quad (2)$$

For melilite and fassaite analyses, multiple standards with variable major elements were analyzed to estimate RSF. There is no obvious change in the RSF among melilite standards including both glasses and a synthetic crystal ($Åk_{15}$- $Åk_{75}$), so that RSF is estimated to be 0.911 with an uncertainty of 1% for melilite. The RSF in 2 fassaite glass standards with lower TiO_2 contents (~2%) were systematically higher than those in other standards (EA2). It is possible that complex mixtures of major elements in fassaite make the RSF more variable than a simple solid solution in melilite. We also applied 1% uncertainty in RSF of spinel analyses (EA2).

2.3.2. Anorthite analyses

For Mg isotope analysis of anorthite, we used mono-collection electron multiplier (EM) in magnetic peak switching mode, while the $^{27}Al^+$ signal was detected using a multicollection FC

detector (with 10^{11} ohm resister) on high mass side simultaneously with the detection of $^{25}Mg^{+}$. Primary beam intensity was ~1.3 nA with 8 μm oval shaped spots (Fig. 2d), using a mass aperture of 100 μm and beam aperture of 400 μm. Due to smaller beam size, the field aperture was set to 4,000 μm square and the regular circular mode was used for the coupling optics. The typical $^{24}Mg^{+}$ and $^{27}Al^{+}$ ions intensities were ~2×10^{5} cps and 5×10^{7}, respectively. Mass resolving power was set to 3,500 (entrance slit of 90 μm and exit slit of 300 μm). Other instrumental parameters are the same as multi-collection FC analyses. A single analysis takes ~30 min, including 400s of presputtering to stabilize Mg ion intensity, ~60s for automated centering of the secondary optics, and 50 cycles of switching between $^{24}Mg^{+}$, $^{25}Mg^{+}$ and $^{26}Mg^{+}$ (counting times of 3s, 10s, and 10s, respectively, with 3s waiting time). We used a natural plagioclase mineral standard with An_{59} composition (Lab1), which was previously used as a standard for Al-Mg dating of chondrules (e.g., Kita et al., 2000; Kurahashi et al., 2008) and has a similar $^{27}Al/^{24}Mg$ ratio (~280) to those in the anorthite of the CAI. Reproducibility of $\delta^{26}Mg^{*}$ values of the plagioclase standard was better than 1‰, although showing a small negative bias of -1.5‰ that was corrected for in unknown samples. The RSF of anorthite is estimated by using measured $^{27}Al/^{24}Mg$ ratios of the Lab1 standard. However, due to its low Mg contents (~0.1 MgO%), the uncertainty of calibration of the $^{27}Al/^{24}Mg$ ratio using EPMA is as large as 6%. Moreover, the major element composition of Lab1 is more Na-rich (An_{59}) than the pure anorthite in the CAI, and therefore the RSF may be different from that of the standard.

More recently, a synthetic anorthite glass standard that is doped with 1.0 wt.% MgO ("AnG+Mg 1%") was available for more precise RSF estimates (Kita et al., 2009b). We compared SIMS measured $^{27}Al/^{24}Mg$ ratios between Lab1 and this anorthite glass standard in three separated Al-Mg sessions in 2009-2010 and found that their ratios were consistent within

252 1%. Thus, the RSF of anorthite applied to the CAI analyses was re-evaluated by using the new
253 anorthite glass standard (see detailed calculation in EA2). Although the $^{27}Al/^{24}Mg$ ratio of
254 AnG+Mg 1% glass is estimated to be 1%, an additional uncertainty based on the comparison of
255 the measured $^{27}Al/^{24}Mg$ ratios between Lab1 and the glass standard of 0.9% (2SD from three
256 sessions) was propagated to the final error estimate. This made the overall uncertainty of the
257 RSFfor anothite in the present study1.3%.
258
259 **3. Results**
260
261 **3. 1. Al-Mg isotope data**
262 The results of the Al-Mg analyses of Leoville 3535-1 Type B1 CAI are shown in Tables
263 1 and 2. We obtained 18 melilite, 8 fassaite, and 9 spinel analyses using multi-FC mode (S1 and
264 S3) and 10 anorthite analyses using mono-EM (S2). Full SIMS data and EPMA data are found
265 intwoelectronic annexes EA2 and EA3, respectively. The locations of the SIMS analyses are
266 shown in electronic annex EA4. Melilite analyses were made in two sessions two years apart, but
267 there are no systematic differences between two data sets. Data from the first session (S1)
268 contain more mantle melilite data than the other (S3). The $^{27}Al/^{24}Mg$ ratios of melilite analyses
269 range from 1.0 to 9.1 and correspond to $Åk_{70}$- $Åk_{20}$, similar to those observed by Knight et al.
270 (2009) for the same CAI. The $^{27}Al/^{24}Mg$ ratios of fassaite analyses show a smaller range of 1-2,
271 which generally correlate with TiO_2 contents. The excess $\delta^{26}Mg^*$ values range from 0.4‰ to 3‰
272 for melilite and from 0.4‰ to 0.8‰ for fassaite. Most of the melilite and all fassaite analyses in
273 the CAI show heavy Mg isotope enrichments after instrumental bias correction with the $\delta^{25}Mg$
274 value of ~5 ‰. The $\delta^{25}Mg$ values of Al-rich melilite ($Åk \leq 30$) at the rim of the CAIs show

slightly lower values as low as 3.5‰.

The spinel analyses were made in multiple locations and textual contexts in the CAI, including spinel in mantle melilite, in other minerals (anorthite, fassaite, and melilite), at the boundary of three minerals (#50), and in spinel aggregates. Because the spinel grains in the CAI are close to pure $MgAl_2O_4$, the $^{27}Al/^{24}Mg$ ratios are constant at 2.59±0.05 (n=9, 2SD), which corresponds to atomic ratio of [Al/Mg] = 2.04±0.04. The excess $\delta^{26}Mg^*$ values are also indistinguishable with an average value of 0.93±0.06‰ (2SD, n=8), except for spot #50 that is at the grain boundary of three minerals in the core ($\delta^{26}Mg^*$=1.08±0.05‰). The $\delta^{25}Mg$ values of spinel analyses show an average of 5.7±0.6‰ that is consistent with those of melilite and fassaite, although the $\delta^{25}Mg$ value of terrestrial spinel standard is not known and assumed to be zero.

The $^{27}Al/^{24}Mg$ ratios of anorthite range from 80 to 360, with most of the data having values of 200-250. The excess $\delta^{26}Mg^*$ values range between 30‰ and 130‰. For most analyses, the $^{27}Al/^{24}Mg$ ratios and $\delta^{26}Mg^*$ values were constant during 50 cylces of analyses of a single spot. However, for spot #10, the ^{24}Mg signal intensities fluctuated between 1.1×10^5 cps and 1.9×10^5 cps, which resulted in the variation of $^{27}Al/^{24}Mg$ ratios between 470 and 280 that correlate with the excess $\delta^{26}Mg^*$ values from 170‰ to 100‰. For this reason, we estimated the error correlation coefficient between $^{27}Al/^{24}Mg$ ratios and the excess $\delta^{26}Mg^*$ values of individual cycles for all the anorthite analyses. As shown in Table 2, the error correlation coefficients were mostly ~0.5 or less, except for spot #10 showing the value of 0.85

3. 2. Al-Mg isochron diagram

The data in Tables 2-3 are ploted as an ^{26}Al-^{26}Mg isochron diagram in Fig. 3. The regression of data using ISOPLOT (Ludwig, 2003) yields well-correlated isochron with the slope

298 0.3590±0.0008 (on $^{27}Al/^{24}Mg$- $\delta^{26}Mg^*$ diagram) with the initial $\delta^{26}Mg^*$ value of 0.056 ±
299 0.081 ‰. The error associate with the slope of the regression line is only 0.2%, though the
300 uncertainties of anorthite and melilite RSF at the level of 1% should be included in the final
301 assessment of the data. The result corresponds to the inferred $^{26}Al/^{27}Al$ ratio of
302 $(5.002\pm0.065)\times10^{-5}$. The MSWD (Mean Square Weighted Deviation) of the regression line is 5.4,
303 which is significantly larger than unity. As shown in Fig. 3b, the Mg-rich data closer to the origin
304 of the isochron show a small amount of scatter around the best-fit line (0.1-0.2‰) that is
305 somewhat larger than the analytical uncertainties (~0.05‰).

306 If a kinetic mass fractionation correction with $\beta = 0.511$ is applied instead of $\beta = 0.514$
307 that was derived from evaporation experiments (Davis et al., 2005), the excess $\delta^{26}Mg^*$ values
308 would be lower by 0.06‰ for a sample with $\delta^{25}Mg = 5$ ‰. Because most data have very similar
309 $\delta^{25}Mg$ (5-6‰), using $\beta = 0.511$ would shift the regression line parallel to the one shown in Fig. 4.
310 This would result in the initial $\delta^{26}Mg^*$ value becoming 0.00 ±0.08 ‰, but the slope of the
311 isochron would not be changed. Data from Al-rich melilite rim have slightly lower $\delta^{25}Mg$ values
312 of 3-4‰ and the excess $\delta^{26}Mg^*$ values using kinetic mass fractionation law would shift the data
313 by only 0.03-0.04‰, which is much smaller than their analytical uncertainties. In fact, the
314 isochron slope estimated from our SIMS data are strongly controlled by the anorthite data with
315 excess $\delta^{26}Mg^*$ values of 80‰ to 130‰, so that the slope of the isochron and the inferred initial
316 $^{26}Al/^{27}Al$ ratio will not be changed by the choice of mass fractionation correction law used to
317 calculate $\delta^{26}Mg^*$.

318 We rejected two anorthite measurements (#2 and #7) from the calculation of the
319 regression line. Inspection of the SIMS spots for these data revealed large cracks and
320 micron-scale inclusions, which are not observed from other analyses spots (Fig. 4). These two

outlier data may have been affected by secondary processes in the parent body, such as impact deformation and shock melting observed from objects in Leoville (e.g., Nakamura et al., 1992; Caillet et al., 1993).

3. 3. Anorthite rim with low Mg content

In this study, three analyses were made from a single anorthite grain (spots #8-10, Fig. 5a) to evaluate sub-solidus Mg isotope diffusion effects that might have disturbed or reset the Al-Mg isotope system. We intentionally aimed one spot at the rim of the grain within 10μm from the boundary adjacent to melilite (spot #10). The $^{27}Al/^{24}Mg$ ratio of #10 was the highest among all the analyses in the CAI and was variable during the 50 cycles of analyses (280-470; Fig. 5b). The result indicates a heterogeneous distribution of Mg in the anorthite at a scale smaller than the depth sampled by a single analysis (~1μm). If there were sub-solidus reheating events for the CAI after the solidification of anorthite, the excess ^{26}Mg that had been accumulated in anorthite would be modified by isotope exchange with isotopically normal Mg during diffusion. The Mg-poor domain of spot #10 should be the first place to see such an effect, because it is close to the grain boundary of an otherwise Mg-rich mineral and has a low Mg concentration. For this reason, we calculated the average $^{27}Al/^{24}Mg$ ratio and $\delta^{26}Mg^*$ value from cycles 27-36 of spot #10, where the ^{24}Mg intensities were lowest (Fig. 5b-c). The average value from the low Mg cycles of spot #10 (here after called #10L) plots exactly on the same isochron with other data (Fig. 5d). The model initial $^{26}Al/^{27}Al$ ratio of the #10L is calculated to be $(5.1\pm0.2)\times10^{-5}$, which is within error from that estimated from the internal isochron of the CAI. The error of the model $^{26}Al/^{27}Al$ ratio (precision ~4%) corresponds to uncertainty of ~40ky in relative age. Thus, Leoville 3535-1 type B1 CAI does not show any evidence of sub-solidus reheating event

344 postdating the crystallization of the CAI by more than 40ky.

345

346 **4. Discussion**

347

348 **4. 1. Relative age of the Leoville 3535-1 type B1 CAI**

349 Multiple bulk CAIs analyses made by Thrane et al. (2006) and Jacobsen et al. (2008)
350 both show well-correlated ^{26}Al-^{26}Mg regression lines, however their inferred initial ^{26}Al/^{27}Al
351 ratios differ by 11%, which much larger than their reported uncertainty. Thrane et al. (2006)
352 reported the initial ^{26}Al/^{27}Al ratios of $(5.85\pm0.05)\times10^{-5}$, while Jacobsen et al. (2008) reported the
353 initial ^{26}Al/^{27}Al ratios of $(5.23\pm0.13)\times10^{-5}$. The latter value for the ^{26}Al/^{27}Al ratio is consistent
354 with the canonical value of 5×10^{-5} (MacPherson et al., 1995). Recent re-evaluations of the bulk
355 CAI isochron by Baker (2008) and Larsen et al. (2010) support the data by Jacobsen et al. (2008).
356 Reanalysis of Vigarano compact type A (CTA) CAI "144A" resulted in the initial ^{26}Al/^{27}Al =
357 $(5.06\pm0.17)\times10^{-5}$ (Connolly et al., 2010), while it was first reported to have the initial ^{26}Al/^{27}Al
358 ratios of $(5.9\pm0.3)\times10^{-5}$ by Young et al. (2005). Thus, recent studies all indicate that the solar
359 system initial ^{26}Al/^{27}Al ratio was similar to the canonical value of 5×10^{-5} that was originally
360 suggested by MacPherson et al. (1995).

361 Recently, MacPherson et al. (2010a; 2010b) reported the ^{26}Al-^{26}Mg data from two
362 pristine fine-grained type A (FTA) CAIs, which are considered to be earliest condensates in the
363 solar nebula. The results show internal ^{26}Al-^{26}Mg isochrons corresponding to initial ^{26}Al/^{27}Al
364 ratios of $(5.27\pm0.17)\times10^{-5}$ and $(5.25\pm0.28)\times10^{-5}$, which are consistent with the bulk CAI
365 isochron by Jacobsen et al. (2008). It is usually assumed that the bulk CAI ^{26}Al-^{26}Mg isochron
366 represents the time when refractory solids first condensed from a well-mixed gas of solar

composition.

The internal ^{26}Al-^{26}Mg isochron of CAI Leoville 3535-1 is interpreted to represent the time when the minerals in this CAI crystallized from a melt. Here we estimate the time of this crystallization relative to the bulk CAI age using the value reported by Jacobsen et al. (2008) as a time anchor and assuming the homogeneous ^{26}Al/^{27}Al ratios in the regions where type B CAIs formed.

$$\Delta t(Ma) = -\tau \ln\left[\frac{\left(^{26}Al/^{27}Al\right)_{\text{L3535-1}}}{\left(^{26}Al/^{27}Al\right)_{\text{Bulk CAI}}}\right] = -1.02 \times \ln\left[\frac{(5.002 \pm 0.065)\times 10^{-5}}{(5.23 \pm 0.13)\times 10^{-5}}\right] \qquad (3)$$

The Eq. (3) gives Δt = 46 ± 29 ky by applying the ^{26}Al half-life of 0.705 million years (Norris et al., 1984; corresponding mean life τ =1.02 Ma). Thus, the final crytallization of Leoville 3535-1 type B1 CAI postdates the time givne by the bulk CAI isochron by ~ 50 ky. The error of the relative age is comparable to the time difference due to the uncertainty of the initial ^{26}Al/^{27}Al ratios of the bulk CAI of about 2.5%.

4. 2. Internal Al-Mg isotope systematics in Leoville 3535-1

In this work, a very precise initial ^{26}Al/^{27}Al ratio was obtained because of the well-correlated isochron data from anorthite with extremely radiogenic Mg isotope ratios (δ^{26}Mg* = 70–130 ‰). Anorthite is amongst the last mineral to crystallize in type B CAI under cooling rate faster than 0.5˚C/hr (e.g., MacPherson et al., 1984; Stolper and Paque, 1986). Therefore, the inferred initial ^{26}Al/^{27}Al ratio obtained in this study represents the time of last melting of the CAI, unless the CAI experienced resetting of ^{26}Al-^{26}Mg system by sub-solidus

heating. Anorthite is especially sensitive to Mg isotope disturbance due to the faster diffusion in anorthite compared to other minerals (LaTourrette and Wasserburg, 1998). Diffusion could have affected the magnesium isotopic composition and/or the Mg/Al ratio during sub-solidus reheating events in the solar nebula (e.g., Young et al., 2005) or during parent body thermal metamorphism. The analysis obtained from the rim of anorthite grain adjacent to melilite (An-#10) show excellent agreement with rest of anorthite analyses, even though Mg concentration in the spot was the lowest among the all analyses and variable within the analytical depth of ~1μm. These anorthite data in Leoville 3535-1 strongly indicate absence of sub-solidus diffusion over a prolonged period since the last melting of the CAI. [NOTE: I think the rim data suggests that there was a redistribution of Mg that gave rise to the variable Mg concentration, but this must have taken place very shortly after the final crystallization of anorthite that the isochron was not affected by the changes in local Mg/Al.]

Ito and Ganguly (2009) compared diffusion rates of Mg among anorthite, spinel, and melilite and concluded that melilite should be the most robust phase for Al-Mg dating of CAIs. MacPherson et al. (2010b) found spinel grains that show large ^{26}Mg excesses up to 3‰ in Vigarano F1 type B CAI. The large excess is found exclusively for spinel grains included in anorthite, in which ^{26}Mg excesses were nearly completely erased by later parent body alteration that associated with the formation of nepheline lamella. On contrast, analyses of spinel grains in melilite and fassaite plot along the isochron made by melilite and fassaite with the canonical ^{26}Al/^{27}Al ratio. They explained unsupported excess ^{26}Mg in spinel as a result of isotope exchange between anorthite and spinel during parent body metamorphism due to fast diffusion of Mg in these minerals, while spinel in melilite and fassaite did not exchange Mg with host mineral due to slow diffusion rate of Mg in the host.

In contrast to Vigarano F1, we do not find any difference among spinel data that are hosted by anorthite, melilite and fassaite in Leoville 3535-1. Anorthite in the CAI is unaltered and does not show thin lamella of nepheline. Therefore, there is no indication of parent body metamorphism that would modify the ^{26}Al-^{26}Mg system of the Leoville 3535-1. Similarly, the internal ^{26}Al-^{26}Mg systematics of Leoville 3535-1 CAI and the data collected closest to the rim does not support this CAI being affected by sub-solidus heating events in the solar nebula that lasted for anything as long the 0.3Ma as had been suggested Young et al. (2005).

While we find the well-defined correlated excess from anorthite data, the MSWD of the isochron fit of all data (~5) is significantly larger than unity, indicating the multi-stage evolution of the ^{26}Al-^{26}Mg system. In Fig. 6, an expanded view of isochron diagram at Mg-rich end is shown. Data scatter significantly beyond analytical uncertainties along the isochron regression line, which resulted in a large MSWD. There seems to be systematic displacement from the regression line depending on mineral phases. Spinel data, except for one, plot below the regression line, while fassaite data plot above the line. Melilite data plot generally on or below the line similar to spinel, but some of most åkermanite-rich melilite plot above the line, similar to fassaite. The coarse-grained texture of Leoville 3535-1 indicates that it experienced a highly molten stage. The displacements of Mg isotope data may relate to the crystallization sequence of minerals, which is in the order of spinel> melilite> fassaite> anorthite (Stolper and Paque, 1986)..The melilite is zoned with increasing åkermanite towards the interio, which indicates that the mantle crystallized inwards from the rim. Stolper and Paque (1986) used expeimental data to argue reheating processes of Type B CAI produced a high degree of partial melting with some fraction of the original spinel having remained while melilite, fassaite and anorthite crystallized as the melt cooled. Because some fraction of the spinel might predate the melting event and

because virtually all the melilite would have crystallized before fassaite and anorthite we calculated two different regression line made by the spinel+melilite data and the fassaite+anorthite data, as shown in Fig. 7. In the calculation of spinel-melilite regression line, four melilite data in the core (#19-20, #43, #46) that plot along with fassaite data were not included. The proportion of åkermanite in these core melilites indicate that they were the last melilites to crystallize, which would have been at much the same as when fassaite and anorthite would have begun to crystallize. Because of this is not entirely surprising that the core melilites plot along with the fassaite data. One mantle melilite data near the rim (#48) and one spinel data (#50- locating at the boundary of multiple minerals, see EA4) are significantly off the isochron and are also excluded from the spinel-melilite regression calculation. The spinel-melilite regression line shows slightly higher initial $^{26}Al/^{27}Al$ ratio of $(5.20\pm0.18)\times10^{-5}$ with relatively low initial $\delta^{26}Mg^* = -0.02\pm0.06‰$, while fassaite- anorthite regression line shows slightly lower initial $^{26}Al/^{27}Al$ ratio of $(4.99\pm0.07)\times10^{-5}$ with relatively higher initial $\delta^{26}Mg^* = 0.13\pm0.03‰$. Although the initial$^{26}Al/^{27}Al$ ratios of two lines are not resolved from each other, spinel-melilite line is steeper and has lower intercept value than those of fassaite-anorthite line. Thus, these data may represent two events, initial formation of type B CAIs and last partial melting event by reheating of the CAI. The initial crystallization of the CAI might occur immediately after the time of bulk CAI isochron, while reheating event continued at the time scale of ~50ky. [NOTE: Given the crytallization sequence one would expect the Spinel and melilite to be older than the fassaite and anorthite - but because of cooling rate considerations (>.1C/hr) there is no way the age difference between Spine-melilite and fassaite-anorthite in a one-stage cooling scenario could have produced the difference of the isochrons. If we accept the isochrons as representing an age difference between the crystallization of these two sets of minerals, then it would have to

458 be the result of multiple stages of heating and partial melting that affected the fassaite and
459 anorthite, but not the more AL-rich melilite.

460 If anorthite crystallized from partial melt while spinel and melilite remained in solid
461 phase, the regression line made by fassaite-anorthite would provide the better estimate of the
462 initial $^{26}Al/^{27}Al$ ratios. Compared to the inferred $^{26}Al/^{27}Al$ ratio of $(5.002\pm0.065)\times10^{-5}$ using all
463 data (Fig. 3), the value of $(4.988\pm0.065)\times10^{-5}$ obtained from fassaite-anorthite regression line is
464 lower only by 0.3% and thus the difference between two regression lines are insignificant. Since
465 the multiple melting processes in type B1 CAI could be very complicated, we consider the
466 regression line using all data as the best estimate of initial $^{26}Al/^{27}Al$ ratio of the Leoville 3535-1
467 CAI.

468

469 **4. 3. Implication to the early history of the solar nebula**

470 In Fig. 8, the initial $^{26}Al/^{27}Al$ ratio of Leoville 3535-1 is compared to the ratio of other
471 type B CAI from CV3 chondrites from recent high precision multi-collector ICP-MS and SIMS
472 analyses (Jacobsen et al., 2008; MacPherson et al., 2010b; Bouvier and Wadhwa, 2010). Four
473 data are from ICP analyses of mineral separates from Allende CAIs (A44A, AJEF, and A43;
474 Jacobsen et al., 2008) and NWA 2364 (Bouvier and Wadhwa, 2010). Another is from SIMS
475 analyses of Vigarano Type B2 CAI F1 that was analyzed during the session S3 of this study
476 (MacPherson et al., 2010b). Uncertainties of the inferred $^{26}Al/^{27}Al$ ratios of these data are much
477 larger (4-8%) than the present work (1.3%) due to the limited range of $^{27}Al/^{24}Mg$ ratios (typically
478 2-8) from mineral separates for ICP analyses and Mg-rich minerals for SIMS analyses. In the
479 case of F1, the isochron regression was made using only Mg-rich minerals due to the anorthite
480 data having been affected by low temperature parent body alteration (MacPherson et al., 2010b).

481 The Leoville 3535-1 data agree very well with three CAIs (A44A, AJEF, and NWA 2364)
482 showing the initial $^{26}Al/^{27}Al$ ratios of 5.0×10^{-5}, which is systematically lower than the bulk CAI
483 data. Thus, major melting events of refractory solids in the solar nebula that formed Type B
484 CAIs may postdate by ~50ky the condensation of their solid precursors. Two other CAI data (F1
485 and A43) have initial $^{26}Al/^{27}Al$ ratios lower than that of Leoville 3535-1. These relatively
486 younger Type B CAIs may indicate that heating events affecting the Type B CAIs continued at
487 least another 0.1Ma.

488 The comprehensive study of pristine CAIs from Vigarano by MacPherson et al. (2010b)
489 that included FTA, CTA (compact type A), Type B, Type C and AOAs found a systematic
490 difference in the inferred $^{26}Al/^{27}Al$ ratios between unmelted and melted CAIs. Melted CAIs
491 generally show a range of $^{26}Al/^{27}Al$ ratios $(4\text{-}5)\times10^{-5}$ and one unusual Type C CAI contains a
492 sub-region with the $^{26}Al/^{27}Al$ ratio 2×10^{-5}, which postdates the bulk CAI isochron by ~1Ma.
493 Therefore, melting of CAIs appears to have continued for as long as 1 Ma, which brings it close
494 to the age of the earliest chondrule formation events.

495 The time scales for the initial condensation of CAI precursors and their subsequent
496 reheating are comparable to the infalling and evolved protostar stages of low mass stars, known
497 as Class 0 and Class 1 objects with typical durations of ~10 ky and ~0.1 Myr, respectively
498 (Feigelson and Montmerle, 1999). During these periods, the accretion rate of circumstellar
499 material to young-sun was high and molecular bipolar flow was active, which would cause high
500 temperature heating events consistent with chemical and isotopic characters of CAIs (e.g.,
501 MacPherson et al., 2005). Ciesla (2010) recently argued that the short interval among ages of
502 CAIs relates to the preservation mechanism of refractory objects in the protoplanetary disk. The
503 refractory inclusions that formed early in the inner disk might spread to outer disk within first the

0.1 Myr, while those formed later period would not be efficiently transported to outer disk. The early-formed CAIs that were spread over the large heliocentric distances might survive until the time of chondrule formation (≥2Ma) and subsequent planetesimal formation. According to his model, the age distribution of CAIs would have a sharp peak at the oldest end. Current available data on type B CAIs show a peak on $^{26}Al/^{27}Al$ ~5.0×10^{-5}, which corresponds to ~50ky after the time of bulk CAI isochron (Fig. 8). Because the Leoville 3535-1 CAI preserved such a well-defined isochron with $^{26}Al/^{27}Al$ =5.0×10^{-5}, this particular CAI would not have experienced the reheating 2Ma later during chondrule formation. Pristine CAIs could have been located in parts of the disk where chondrule formation process was not efficient, but eventually incorporated to the CV chondrite parent asteroid. More analyses of various types of pristine CAIs by in-situ high precision SIMS technique will help to better constrain the environments of their formation, the nature of energetic processes that reheated then and the transport of solid in the proto-planetary disk.

5. Conclusions

The high-precision SIMS ^{26}Al-^{26}Mg analyses of the pristine Type B1 CAI Leoville 3535-1 show a well-defined isochron with the initial $^{26}Al/^{27}Al$ =$(5.002\pm0.065)\times10^{-5}$. The analyses of anorthite near the boundary with melilite show variable $^{27}Al/^{24}Mg$ ratios of 280-470 and yet plot exactly on the same isochron. We conclude that the CAI did not experience sub-solidus diffusion that affected the Al-Mg system much after the last melting event. Assuming the homogeneous distribution of ^{26}Al in the solar system, the Leoville 3535-1 Type B1 CAI last melted ~50ky after the time of the bulk CAI isochron, which most likely represents

527 the condensation of refractory solids in the earliest solar nebula. A small (~0.1‰) scatter of the
528 Mg isotope ratios from the regression line is observed in Mg-rich minerals, especially spinel and
529 fassaite being below and above the regression line, respectively. Spinel and Al-rich melilite
530 could be solid residues that survived the partial melting of the CAI precursor, while fassaite and
531 anorthite crystallized from the melt. Two separate isochron regression lines were calculated for
532 spinel-melilite and fassaite-anorthite with the initial $^{26}Al/^{27}Al$ values of $(5.20\pm0.18)\times10^{-5}$ and
533 $(4.99\pm0.07)\times10^{-5}$, respectively. While these two isochron ages are not resolvably different, it is
534 possible that Leoville 3535-1 Type B1 CAI with a zoned melilite mantle first formed from nearly
535 total melt immediately after the time of bulk CAI isochron [NOTE: If the spinel and melilite that
536 did not remelt has an isochrom age that is about 50 Ky older that the bulk CAI age, why are you
537 arguing that it formed "immesdiately after the time of bulk CAI. It seems to me that what one
538 can say is that the spinel- melilite age refers to a high degree of melting event and that a very
539 short time later (barely resolvable, but you can put a bound on it) the CAI was partially remelted
540 affecting only the fassaite, anorthite and the most Mg -rich melilite.] . Later reheating of the CAI
541 resulted in partial melting that occurred ~50ky later.

542 The highly precise and accurate SIMS Al-Mg isotope analysis of CAIs is a powerful
543 means of resolving relative time differences of their formation as short as 10ky. More studies on
544 a variety of pristine CAIs combining petrographic, chemical, and isotope analyses will provide
545 very valuable insights into the earliest history of the Solar System on time scales of 0.1 Myr or
546 less.

547

548 **Acknowledgements** We thank Glenn MacPherson, Smithsonian Institute, for the use of Leoville
549 3535-1 sections and helpful discussions. Brian Hess and Jim Kern are acknowledges for

preparation of SIMS standard mounts and technical assistance to SIMS operations, respectively. This work is supported by NASA Cosmochemistry Program (NNX07AI46G, NK; **NNX09AG38G, FMR;**) and Origin of the Solar System Program (NNX09AB88G; NK). WiscSIMS is partly supported by NSF (EAR03-19230, EAR07-44079). This work performed under the auspices of the U.S. Department of Energy by Lawrence Livermore National Laboratory under Contract DE-AC52-07NA27344 (KK).

Electronic Annex

EA1: List Mg isotope standards

EA2: Detailed SIMS Al-Mg isotope analyses data of Leoville 3535-1

EA3: EPMA analyses of melilite and fassaite in Leoville 3535-1

EA4: Locations of SIMS analyses in Leoville 3535-1

References

Amelin Y., Krot A. N., Hutcheon I.D. and Ulyanov A. A. (2002) Lead isotopic ages of chondrules and calcium-aluminum-rich inclusions. *Science* **297**, 1678-1683.

Baker J.A. (2008) High-precision Al-26-Mg-26 dating solid and planetesimal formation in the young Solar System. *Geochim. Cosmochim. Acta Suppl*. **72**, A45.

Bizzarro M., Baker J. A. and Haack H. (2004) Mg isotope evidence for contemporaneous formation of chondrules and refractory inclusions. *Nature* **431**, 275-278.

Bizzarro M., Baker J. A., and Haack H. (2005) Corrigendum for Mg isotope evidence for

573 contemporaneous formation of chondrules and refractory inclusions. *Nature* **435**, 1280.
574 Bouvier A. and Wadhwa M. (2010). The age of the Solar System redefined by the oldest Pb–Pb
575 age of a meteoritic inclusion. *Nature Geoscience* **3**, 637-641.
576 Caillet C., MacPherson G. J., and Zinner E. K. (1993) Petrologic and Al-Mg isotopic clues to the
577 accretion of two refractory inclusions onto the Leoville parent body - One was hot, the other
578 wasn't. *Geochim. Cosmochim. Acta* **57**, 4725-4743.
579 Catanzoaro E. J., Murphy T. J., Garner E. L. and Shields W. R. (1966) Absolute isotopic
580 abundance ratios and atomic weights of magnesium. *J. Res. Natl. Bur. Stand*. **70a**, 453–458.
581 Ciesla F. J. (2007) Outward transport of high-temperature materials around the midplane of the
582 solar nebula. Science 318, 613-615.
583 Ciesla F. J. (2010) The distributions and ages of refractory objects in the solar nebula *Icarus* **208**,
584 455–467.
585 Clayton R. N., Grossman L., and Mayeda T. K. (1973) A Component of Primitive Nuclear
586 Composition in Carbonaceous Meteorites. *Science* **182**, 485-488.
587 Connelly J. N., Amelin Y., Krot A. N. and Bizzarro M. (2008) Chronology of the solar system's
588 first solids. *Astrophys. J.* **675**, L121–L124.
589 Connolly H. C., Young E. D., Huss G. R., Nagashima K., McDonough W. F, Ash R. D., Beckett
590 J. R., Tonui E. and McCoy T. J. (2009) Supra-Canonical 26Al Detected by In Situ
591 LA-MC-ICPMS and SIMS Techniques: But What Does It All Mean?. *Lunar Planet. Sci.*
592 *Conf.* **40**, abstr. #1993.
593 Connolly, H. C., Young, E. D., Huss, G. R., Nagashima, K., Beckett, J. R., and McCoy, T. J.
594 (2010) To Be or Not To Be Canonical, What's New? The Search for the Initial 26Al
595 Abundance of the Solar System. Lunar Planet. Sci. Conf. 41, abstr. #1933.

596 Cosarinsky M., Taylor D. J., Liu M. C., McKeegan K. D., and Krot A. N. (2007) Distribution of
597 Aluminum-26 in Refractory Inclusions from CV Chondrites. Contribution No. 1374,
598 p.48-49.
599 Cuzzi J. N., Davis S. S. and Dobrovolskis A. R.. (2003) Blowing in the wind. II. Creation and
600 redistribution of refractory inclusions in a turbulent protoplanetary nebula. Icarus, 166,
601 385-402.
602 Davis A. M., Richter F. M., Mendybaev R. A., Janney P. E., Wadhwa M., McKeegan K. D.
603 (2005) Isotopic mass fractionation laws and the initial solar system $^{26}Al/^{27}Al$ ratio. Lunar
604 Planet. Sci. Conf. 36, abstract #2334.
605 Fagan T. J., Guan Y., and MacPherson G. J. (2007) Al-Mg isotopic evidence for episodic
606 alteration of Ca-Al-rich inclusions from Allende. *Meteorit. Planet. Sci.* **42**, 1221-1240.
607 Feigelson E. D. and Montmerle T. (1999) High-energy processes in young stellar objects. *Annu.*
608 *Rev. Astron. Astrophys.* **37**, 363–408.
609 Grossman L. (1972) Condensation in the primitive solar nebula. Geochim. Cosmochim. Acta, 36,
610 597-619.
611 Ito, M. and Ganguly, J. (2009) Mg Diffusion in Minerals in CAIs: New Experimental Data for
612 Melilites and Implications for the Al-Mg Chronometer and Thermal History of CAIs. Lunar
613 Planet. Sci. Conf. 40, Abstr. #1753.
614 Jacobsen B., Yin, Q-Z, Moynier F., Amelin Y., Krot AN, Nagashima K., Hutcheon, I and Palme,
615 H. (2008) ^{26}Al-^{26}Mg and ^{207}Pb-^{206}Pb systematics of Allende CAIs: Canonical solar initial ^{26}
616 $Al/^{27}Al$ ratio reinstated. Earth Planet. Sci. Lett. 272, 353-364.
617 Kita, N.T., Nagahara, H., Togashi, S. and Morishita, Y. (2000) A short duration of chondrule
618 formation in the solar nebula: evidence from 26Al in Semarkona ferromagnesian chondrules.

619 Geochim. Cosmochim. Acta 64, 3913-3922.
620 Kita NT, Ushikubo T, Fu B and Valley JW (2009a). High precision SIMS oxygen isotope
621 analysis and the effect of sample topography. Chemical Geology 264(1-4): 43-57.
622 Kita N, Fournelle J, Mendybaev R, Knight K, Davis AM, Richter FM and Ushikubo T (2009b).
623 Evaluation of anorthite glass standards for high precision SIMS Al-Mg dating of early solar
624 system materials. Eos Trans. AGU 90 (52) Fall Meet. Suppl., Abstract V31E-2020.
625 Knight, K. B., Kita, N. T., Davis, A. M., Richter, F. M., and Mendybaev, R. A., 2009. Mg and Si
626 Isotope Fractionation Within Three Type B Ca-Al-rich Inclusions. *Lunar Planet. Sci.* 40,
627 Abstr. # 2360.
628 Kurahashi, E., Kita, N. T., Nagahara, H., and Morishita, Y., 2008. Al-26-Mg-26 systematics of
629 chondrules in a primitive CO chondrite. Geochim. Cosmochim. Acta 72, 3865-3882
630 Larsen K., Trinquier A., Paton C., Ivanova M., Nordlund Å, Krot AN and Bizzarro M. (2010)
631 Heterogeneous distribution of ^{26}Al in the solar protoplanetary disk, Meteorit. Planet. Sci.
632 Suppl. 45, A113.
633 LaTourrette T. and Wasserburg G. J. (1998) Mg diffusion in anorthite: implications for the
634 formation of early solar system planetesimals. Earth Planet. Sci. Lett. 158, 91–108.
635 Lee T., Papanastassiou D. A., and Waserburg G. J. (1977) Aluminum-26 in the early solar
636 system – Fossil or Fuel. Astrophys. J., 211, L107-110.
637 Liermann H.P. and Ganguly J. (2002) Diffusion kinetics of Fe^{2+} and Mg in aluminous spinel:
638 Experimental determination and applications. Geochim. Cosmochim. Acta 66, 2903-2913.
639 Ludwig K. R. (2003) Isoplot 3.00 A geochronological toolkit for Microsoft excel. Berkeley
640 Geochronology Center Special Publication No.4, 1–72.
641 MacPherson G. J., Davis A. M. and Zinner E. K. (1995) The distribution of aluminum-26 in the

642 early solar system: a reappraisal. Meteoritics 30, 365–386.
643 MacPherson G. J., Simon S. B., Davis A. M., Grossman L., and Krot A. N. (2005)
644 Calcium-Aluminum-rich Inclusions: Major Unanswered Questions. In Chondrites and the
645 Protoplanetary Disk (Eds. Krot, A.N., Scott, E.R.D. and Reipurth, B.), ASP Conference
646 Series, 341, pp. 225-250. Astronomical Society of the Pacific, San Francisco.
647 MacPherson GJ, Bullock ES, Jenny PE, Kita NT, Ushikubo T, Davis AM, Wadhwa M and Krot
648 AN (2010a). Early solar nebula condensates with canonical, not supracanonical, initial
649 $^{26}Al/^{27}Al$ ratios. Astrophys. J. 711, L117-L121.
650 MacPherson GJ, Kita NT, Ushikubo T, Bullock ES and Davis AM (2010b). High-precision
651 $^{26}Al/^{27}Al$ isochron microchronology of the earliest solar system. Lunar Planet. Sci. 41, Abstr.
652 #2356.
653 McKeegan K. D., Larzebinski G. J., Kallio A. P., Mao P. H., Coath C. D., Kunihiro T., Wiens R.
654 C., Allton J. H., Callaway M., and Rodriguez M. C. (2008) A First Look at Oxygen in
655 Genesis Concentrator Sample. Lunar Planet. Sci. 39, abstract# 2020.
656 McKeegan K. D., and 46 co-authors (2006) Isotopic Compositions of Cometary Matter Returned
657 by Stardust. Science, 314, 1724-1728.
658 Nakamura T., Tomeoka K., and Takeda H. (1992) Shock effects of the Leoville CV
659 carbonaceous chondrite - A transmission electron microscope study. Earth Planet. Sci. Lett.
660 114, 159-170.
661 Norris T. L., Gancarz A. J., Rokop D. J., Thomas K. W. (1983) Half-life of ^{26}Al. *Proc. 14th*
662 *Lunar Planet. Sci. Conf., J. Geophys. Res.* **88** (1983) B331.
663 Podosek F. A., Zinner E. K., MacPherson G. J., Lundberg L. L., Brannon J. C., and Fahey A. J.
664 (1991) Correlated study of initial $^{87}Sr/^{86}Sr$ and Al-Mg systematics and petrologic properties

665 in a suite of refractory inclusions from the Allende meteorite. Geochim. Cosmochim. Acta,
666 55, 1083-1110.
667 Richter F. M, Kita N. T., Mendybaev R. A., Davis A. M. and Valley J. W. (2007) High-precision
668 Mg isotopic composition of Type B1 and B2 CAI melilite. Lunar Planet. Sci. Conf. 38,
669 Abstract #2303
670 Shu FH, Shang H, Lee T. (1996) Toward an astrophysical theory of chondrites. Science 277,
671 1475-1479.
672 Stolper E. and Paque J. M. (1986) Crystallization sequences of Ca-Al-rich inclusions from
673 Allende: The effects of cooling rate and maximum temperature. Geochim. Cosmochim.
674 Acta 1986, 1785-1806.
675 Thrane K, Bizzarro M and Baker JA (2006) Extremely brief formation interval for refractory
676 inclusions and uniform distribution of Al-26 in the early solar system. ApJ. 646, L159-162.
677 Valley JW and Kita N (2009). In situ Oxygen Isotope Geochemistry by Ion Microprobe.
678 Mineralogical Association of Canada Short Course 41, Toronto, May 2009: 19-63.
679 Young E. D., Simon J. I., Galy A, Russell S. S., Tonui E., and Lovera O. (2005) Supra-canonical
680 $^{26}Al/^{27}Al$ and the residence time of CAIs in the solar protoplanetary disk. Science 308,
681 223-227.
682 Zolensky M. E, and 74 co-authors (2006) Mineralogy and Petrography of Comet 81P/Wild 2
683 Nucleous Sample. Science, 314, 1735-1739.
684

685 **Figure Caption**

686

687 Fig. 1. Back scattered images (BES) of Leoville 3535-1 Type B1 CAI (a) The image of whole
688 CAI. A rectangle indicates the area shown as an expanded view in (b). (b) Expanded view of the
689 CAI including the ~500μm thick melilite (Mel) mantle. Core of the CAI consists of euhedral
690 melilite (Mel), fassaite (FAS) and anorthite (An). Small grains of spinel (≤50μm) are distributed
691 throughout the inclusion.

692

693 Fig. 2. Examples of SIMS spots in different minerals (shown as BSE images). (a) Melilite, (b)
694 fassaite, (c) spinel, and (d) anorthite. Scale bars are 20μm for (a-c) and 10μm for (d). Melilite
695 and fassaite analyses were made using 20nA O^- primary ions, and the BES shows a 25×20 μm
696 oval beam spot with a surrounding area ~40×50μm where the surface carbon coating was
697 removed. Spinel analyses were made using 5-7nA primary beam with ~25μm well-defined flat
698 bottom pits, although the edge of beam (partly shown as a dashed line) often overlaps with grain
699 boundaries. Anorthite analyses were made using 1nA primary beam resulting in ~8μm flat
700 bottom pits.

701

702 Fig. 3. ^{26}Al-^{26}Mg isochron diagram of Leoville 3535-1. (a) anorthite data, (b) Mg-rich mineral
703 data. Anorthite data ppints #2 and #7 are off the linear trend and were not included when
704 determining the slope of the isochron. The dashed line in (b) indicates 2σ (?)error limits of the
705 regression line.

706

707 Fig. 4. Back scaerred electron images used to examine the SIMS pits that were produced by the

anorthite analyses. The two data points that are off the regression line in Fig. 3 (#2 and #7) have irregular SIMS pits, indicating possible disturbance by secondary processes in the parent body. The scale bar = 10μm.

Fig. 5. The anorthite analysis at the rim adjacent to melilite (#10). (a) Location of analyses. Two other spots (#8 and #9) were obtained in the same grain near the center. (b) Variation of ^{24}Mg intensity and $^{27}Al/^{24}Mg$ ratios within a single analyses (50 cycles). Cycles 27-36 (shown as grey) show the highest $^{27}Al/^{24}Mg$ ratios. (c) the excess $\delta^{26}Mg^*$ of individual cycles, showing highest values at cycles 27-36. (d) The average data from cycles 27-36 plot ("An#10L") on the isochron diagram. The two other spots in the same anorthite grain (#8 and #9) have lower $^{27}Al/^{24}Mg$ ratios similar to other analyzed anorthite grains. The grey line represents a regression line of all data excluding anorthite #10. The data for An#10L plots on the same isochron as the rest of data. The average of all 50 cycles of spot #10 (An-#10) is shown as an error ellipse for comparison with the regression line defined by the other anorthite data points..

Fig. 6. Comparison of the ^{26}Al-^{26}Mg data for spinel, melilite, and fassaite with low $^{27}Al/^{24}Mg$ ratios (<3). The solid and dashed lines are the regression line and error limits shown in Fig. 3(b). Data show significant scatter beyond analytical uncertainties. With only a few exceptions, the spinel data plot below and the fassaite data plot above the regression line.

Fig. 7. Two isochron regression lines from spinel-melilite data (grey) and fassaite-anorthite data (black). Anorthite data are used to calculate the regression line but are not shown in this figure. Several data from spinel and melilite shown as filled symbols were not used in the calculation of

731 the regression line. Most of these data plot closer to fassaite-anorthite line than the line defined
732 by the other spinel and melilite data..
733
734 Fig. 8. A compilation of the initial $^{26}Al/^{27}Al$ ratios of individual Type B CAIs from internal
735 isochron regressions. Leoville 3535-1 is from this work. Data sources for the other Type B CAIs:
736 A44, AJEF, and A43 (from Allende, Jacobsen et al., 2008); F1 (from Vigarano, MacPherson et
737 al., 2010b); NWA 2364 (Bouvier and Wadhwa, 2010). The bulk CAI isochron of Jacobsen et al.
738 (2008) and the internal isochrons of two fluffy Type A (FTA MacPherson et al., 2010a; 2010b)
739 show systematically higher initial $^{26}Al/^{27}Al$ ratios than Type B CAIs.

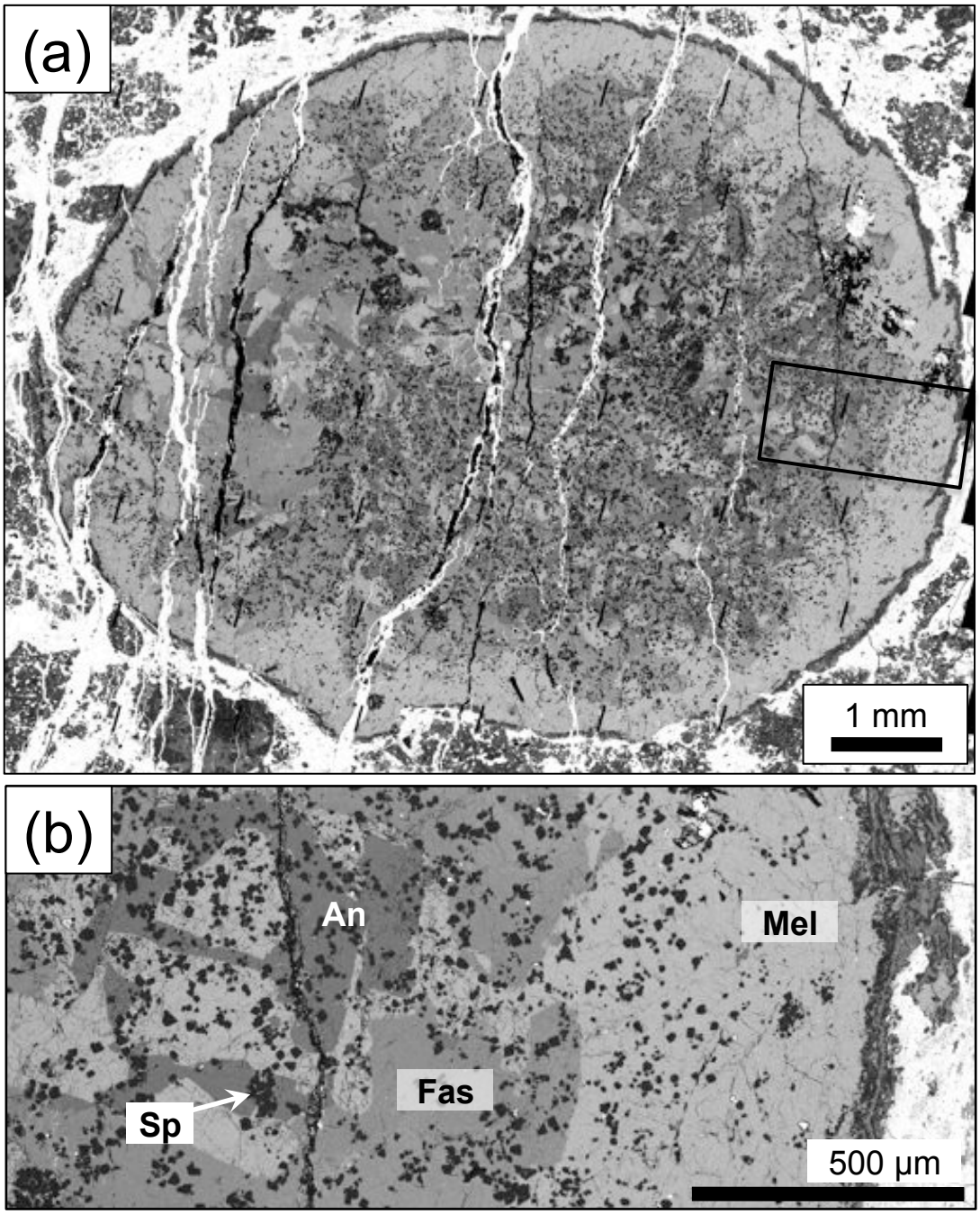

Fig. 1

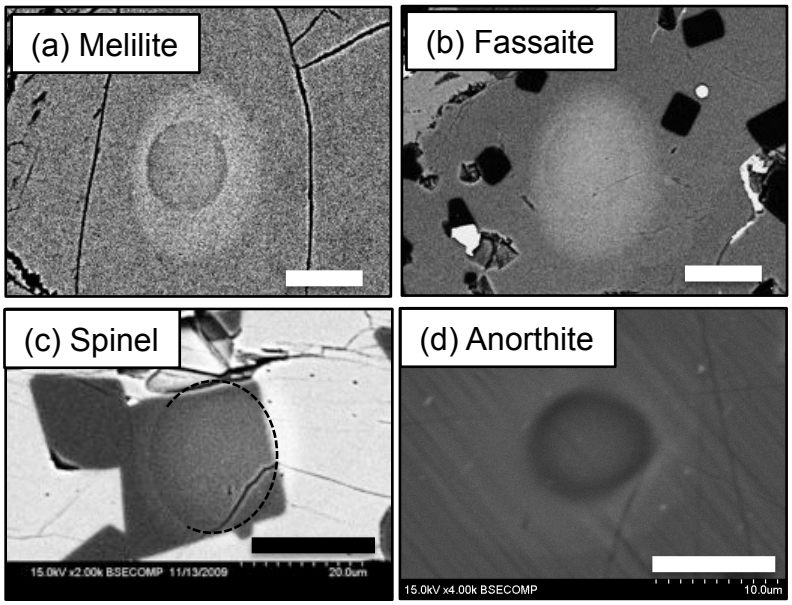
(a) Melilite
(b) Fassaite
(c) Spinel
(d) Anorthite
15.0kV x2.00k BSECOMP 11/13/2009
20.0um
15.0kV x4.00k BSECOMP
10.0um

Fig. 2

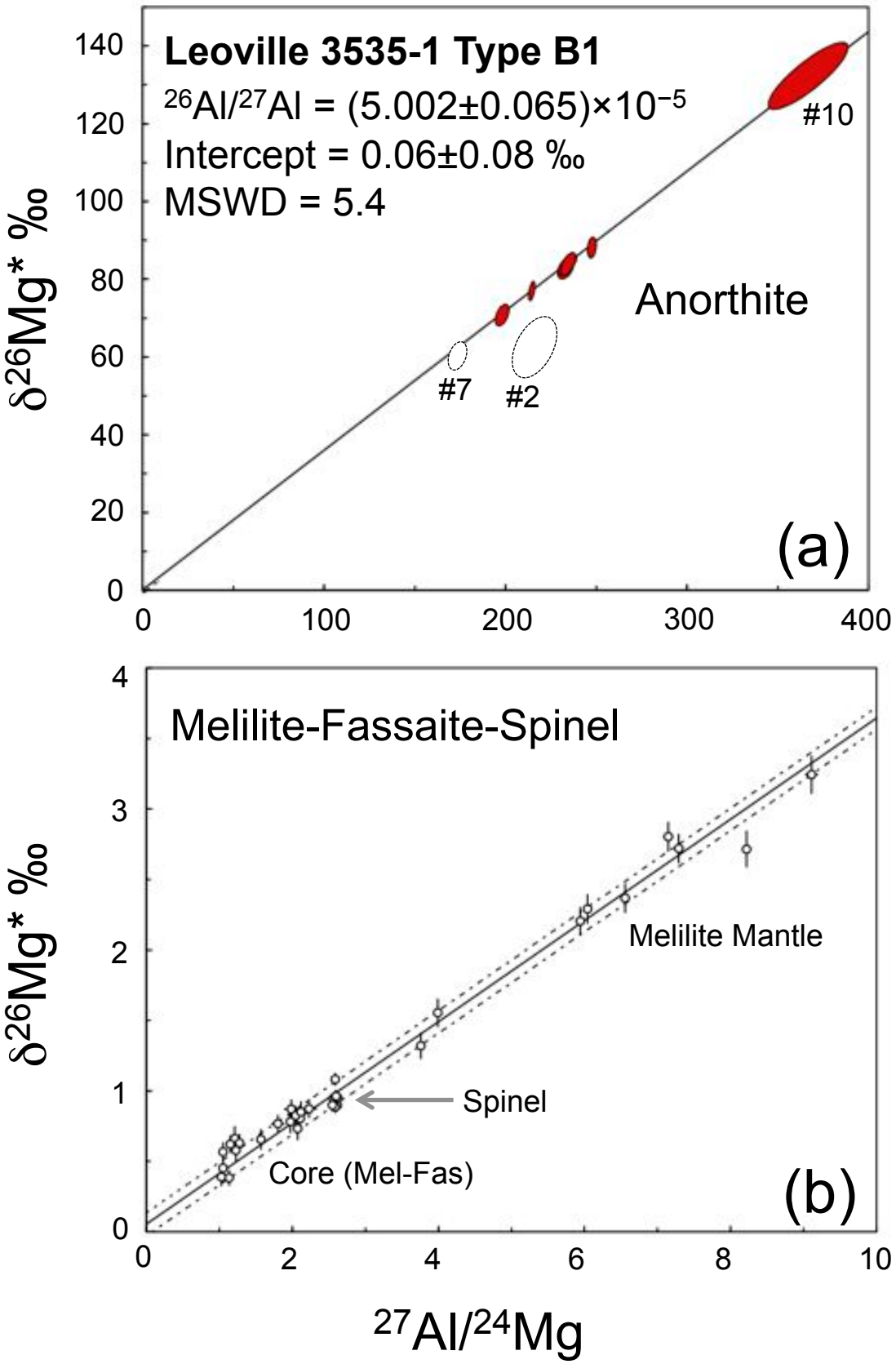
Leoville 3535-1 Type B1
$^{26}Al/^{27}Al = (5.002\pm0.065)\times10^{-5}$
Intercept = 0.06±0.08 ‰
MSWD = 5.4
#10
Anorthite
#7
#2
(a)
$\delta^{26}Mg^*$ ‰
Melilite-Fassaite-Spinel
Melilite Mantle
Spinel
Core (Mel-Fas)
(b)
$^{27}Al/^{24}Mg$

Fig. 3

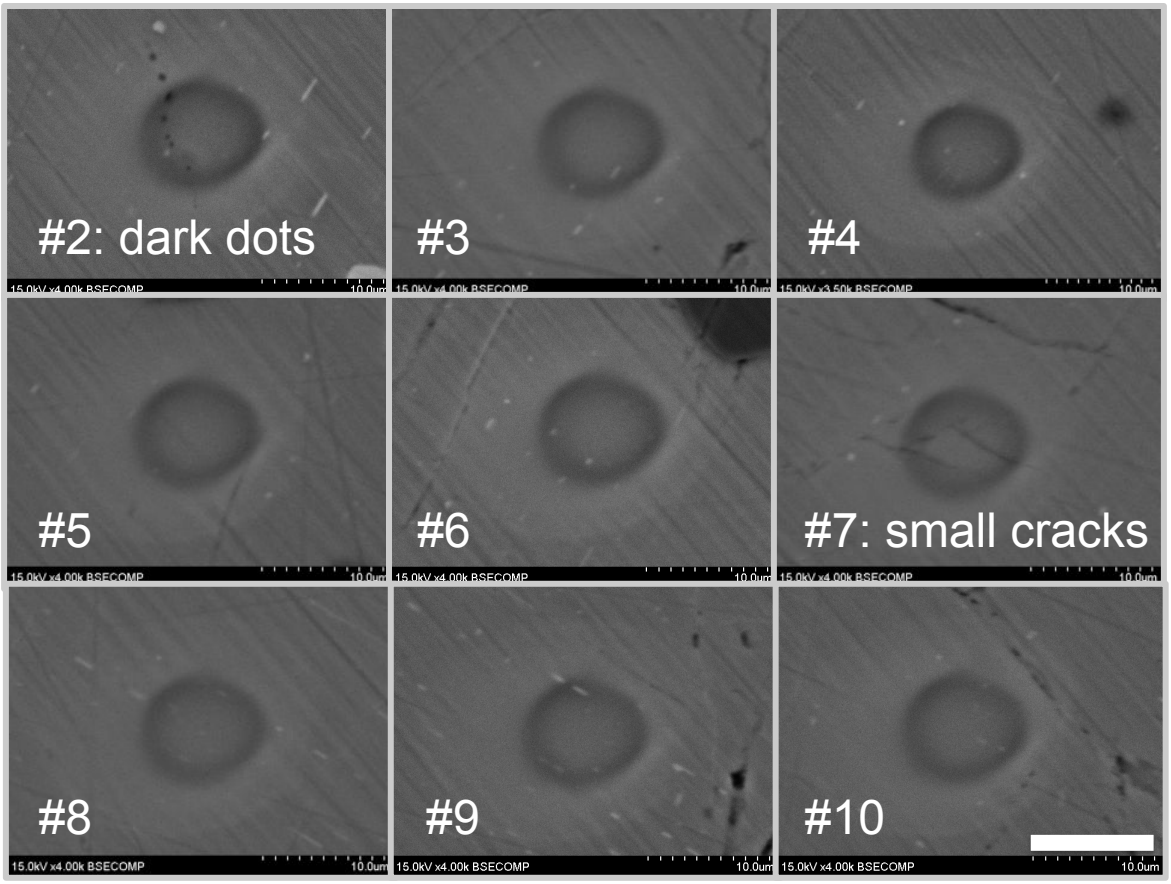
#2: dark dots
#3
#4
#5
#6
#7: small cracks
#8
#9
#10
15.0kV x4.00k BSECOMP
10.0um

Fig. 4

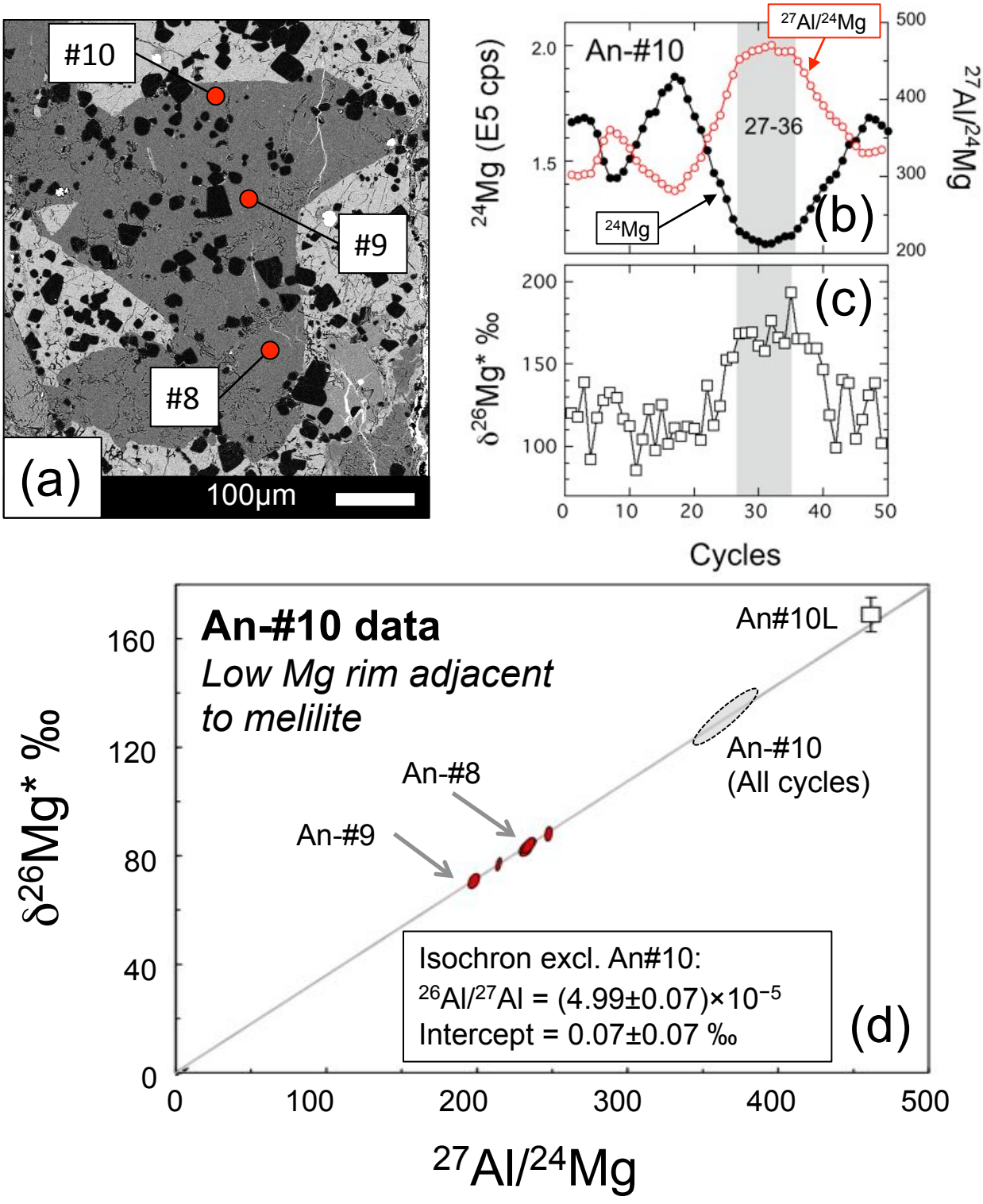
#10
#9
#8
(a)
100μm
An-#10
^{27}Al/^{24}Mg
27-36
^{24}Mg
(b)
(c)
^{24}Mg (E5 cps)
^{27}Al/^{24}Mg
δ^{26}Mg* ‰
Cycles
An-#10 data
Low Mg rim adjacent to melilite
An#10L
An-#10 (All cycles)
An-#8
An-#9
Isochron excl. An#10:
^{26}Al/^{27}Al = (4.99±0.07)×10^{-5}
Intercept = 0.07±0.07 ‰
(d)
δ^{26}Mg* ‰
^{27}Al/^{24}Mg

Fig. 5

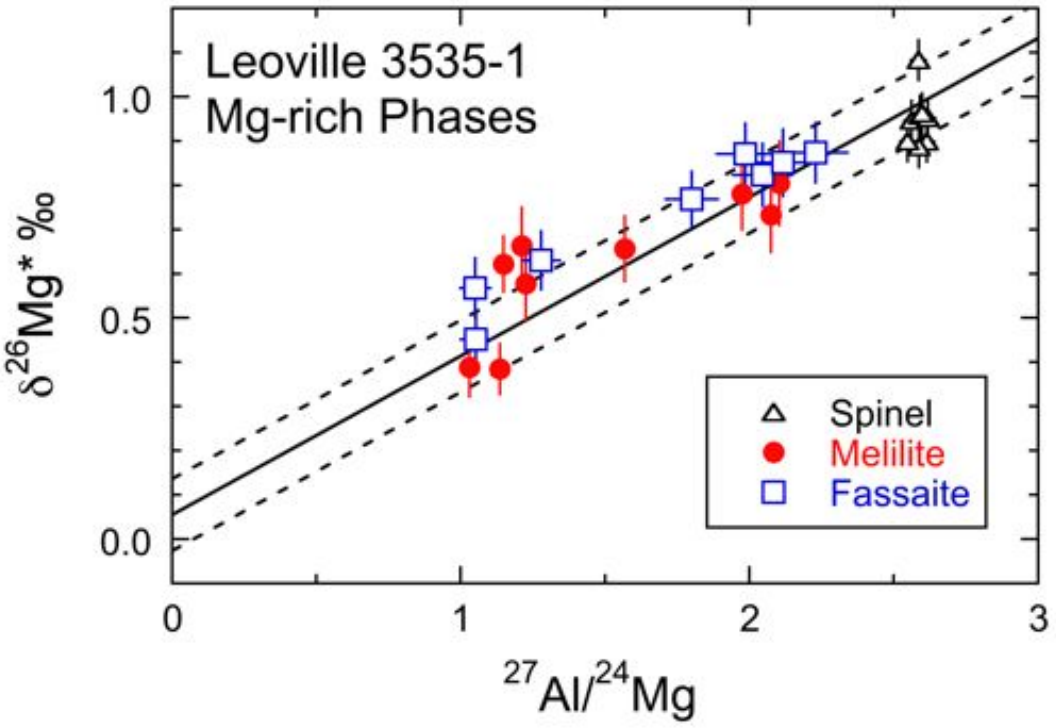
Leoville 3535-1
Mg-rich Phases
Spinel
Melilite
Fassaite
1.0
0.5
0.0
0
1
2
3
δ26Mg* ‰
27Al/24Mg

Fig. 6

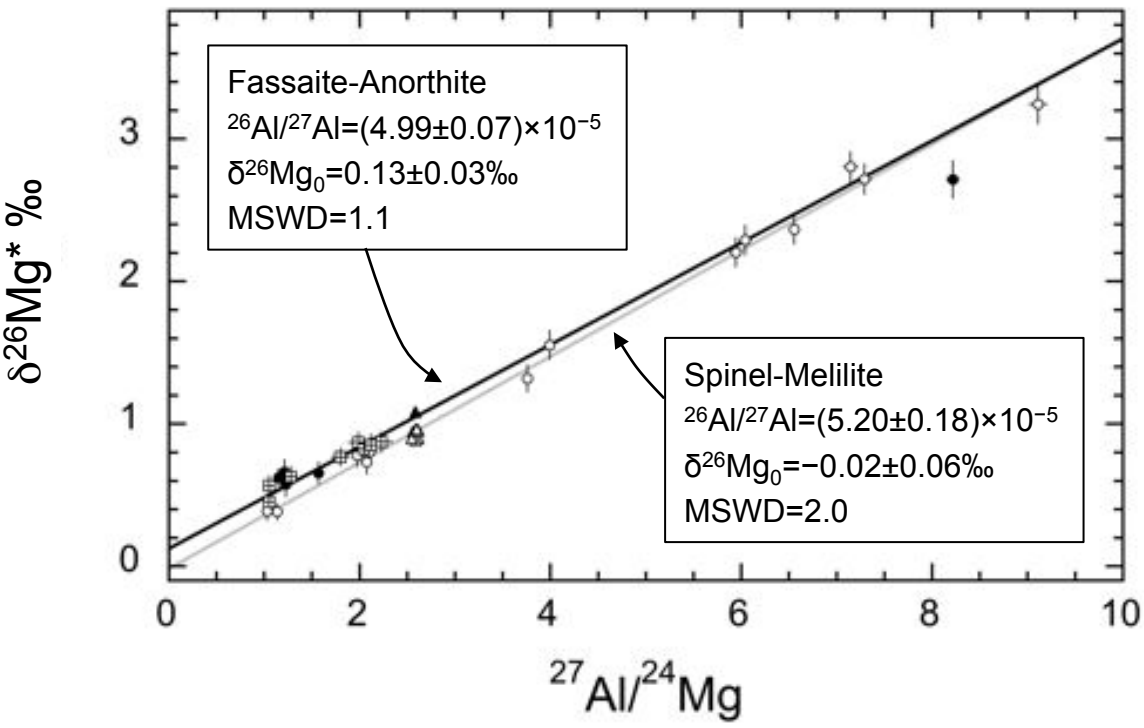
Fassaite-Anorthite
$^{26}Al/^{27}Al=(4.99\pm0.07)\times10^{-5}$
$\delta^{26}Mg_0=0.13\pm0.03‰$
MSWD=1.1
Spinel-Melilite
$^{26}Al/^{27}Al=(5.20\pm0.18)\times10^{-5}$
$\delta^{26}Mg_0=-0.02\pm0.06‰$
MSWD=2.0
$\delta^{26}Mg^*$ ‰
$^{27}Al/^{24}Mg$
0
1
2
3
0
2
4
6
8
10

Fig. 7

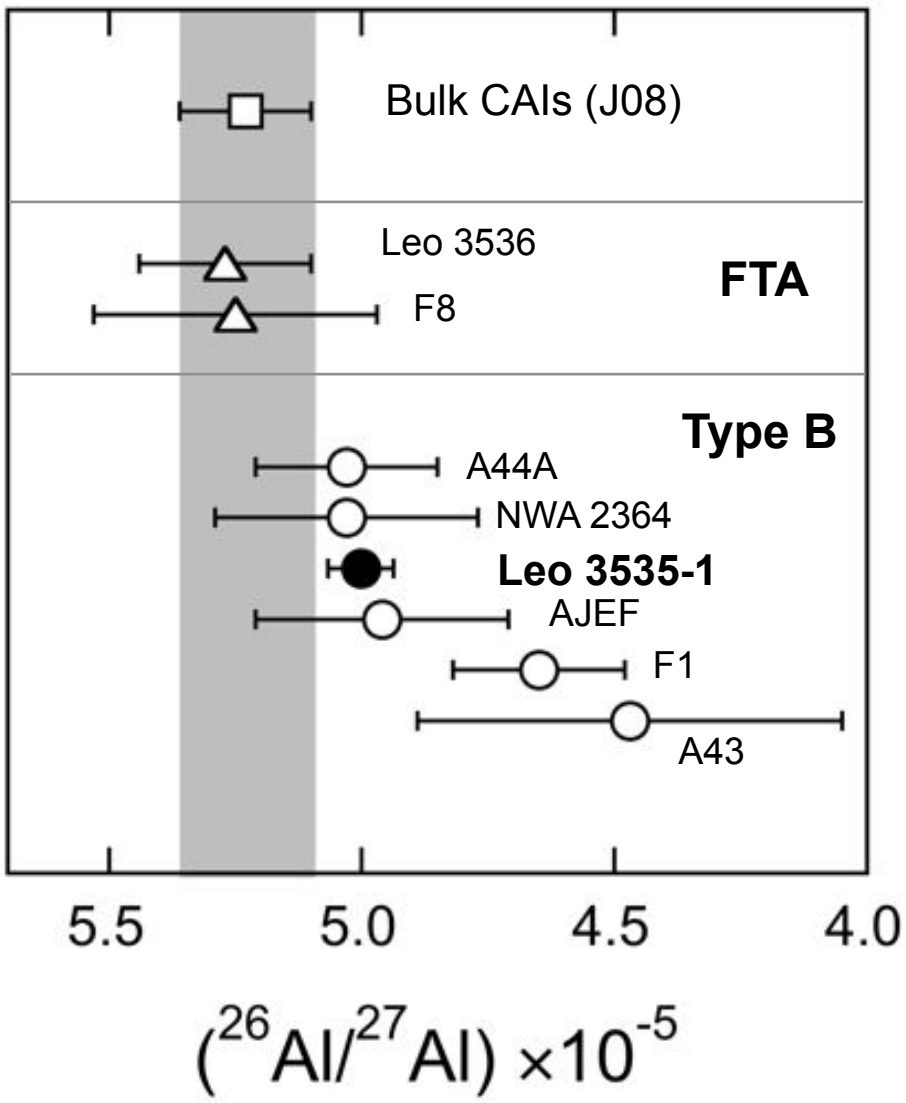
Bulk CAIs (J08)
Leo 3536
F8
FTA
Type B
A44A
NWA 2364
Leo 3535-1
AJEF
F1
A43
5.5
5.0
4.5
4.0
(26Al/27Al) ×10-5

Fig. 8

Table 1. The Al-Mg isotope analyses of melilite, fassaite, and spinel in Leoville 3535-1 type B1 CAI.

Analyses Number	$^{27}Al/^{24}Mg$	2SE	$\delta^{26}Mg^*$ ‰	2SE ‰	$\delta^{25}Mg$ ‰	2SD ‰
Session 1 (2007 July)						
Melilite core -#19	1.23	0.01	0.577	0.084	5.52	0.07
Melilite core -#20	1.21	0.01	0.663	0.087	5.53	0.07
Melilite mantle -#21	2.10	0.02	0.805	0.095	5.62	0.07
Melilite mantle -#22	3.99	0.04	1.554	0.102	5.08	0.07
Melilite mantle -#23	6.04	0.06	2.290	0.105	3.66	0.07
Melilite mantle -#24	7.29	0.07	2.719	0.105	5.30	0.07
Melilite mantle -#25	5.94	0.06	2.205	0.101	5.21	0.07
Melilite mantle -#26	7.15	0.07	2.804	0.106	4.45	0.07
Melilite mantle -#27	9.11	0.09	3.243	0.136	3.71	0.07
Session 3 (2009 September)						
Melilite mantle -#41	1.97	0.02	0.780	0.081	5.35	0.12
Melilite mantle -#42	3.76	0.03	1.320	0.095	5.12	0.12
Melilite mantle -#43	1.57	0.01	0.656	0.074	5.61	0.12
Melilite core -#44	1.14	0.01	0.384	0.057	5.07	0.12
Melilite core -#45	1.03	0.01	0.389	0.066	5.15	0.12
Melilite core -#46	1.15	0.01	0.622	0.063	5.36	0.12
Melilite mantle -#47	6.56	0.05	2.367	0.105	4.63	0.12
Melilite mantle -#48	8.22	0.07	2.715	0.131	3.50	0.12
Melilite mantle -#49	2.07	0.02	0.733	0.084	5.10	0.12
Fassaite -#59 (TiO_2=8.0%)	2.23	0.11	0.874	0.067	5.09	0.25
Fassaite -#60 (TiO_2=5.5%)	1.99	0.10	0.871	0.069	4.79	0.25
Fassaite -#61 (TiO_2=2.8%)	1.05	0.05	0.567	0.067	4.34	0.25
Fassaite -#62 (TiO_2=2.5%)	1.05	0.05	0.452	0.064	4.45	0.25
Fassaite -#63 (TiO_2=4.2%)	1.80	0.09	0.768	0.062	5.08	0.25
Fassaite -#64 (TiO_2=8.6%)	2.05	0.10	0.824	0.070	5.17	0.25
Fassaite -#65 (TiO_2=5.1%)	1.28	0.06	0.631	0.066	4.86	0.25
Fassaite -#66 (TiO_2=7.6%)	2.12	0.11	0.851	0.076	5.07	0.25
Spinel- #47 (fassaite)	2.56	0.03	0.946	0.045	5.76	0.03
Spinel- #48 (melilite mantle)	2.62	0.03	0.899	0.045	5.47	0.03
Spinel- #49 (anorthite)	2.59	0.03	0.886	0.045	6.19	0.03
Spinel- #50 (core)	2.59	0.03	1.083	0.045	5.72	0.03
Spinel- #51 (anorthire in core)	2.60	0.03	0.957	0.045	5.55	0.03
Spinel- #52 (fassaite in core)	2.55	0.03	0.899	0.045	5.50	0.03
Spinel- #53 (fassaite)	2.59	0.03	0.958	0.045	5.96	0.03
Spinel- #54 (spinel aggregates)	2.62	0.03	0.952	0.045	5.93	0.03
Spinel- #55 (spinel aggregate)	2.60	0.03	0.962	0.045	5.66	0.03

Table 2. The Al-Mg isotope analyses of anorthite in Leoville 3535-1 type B1 CAI.

Analyses Number	$^{27}Al/^{24}Mg$	2SE	d(^{26}Mg)* ‰	2SE ‰	Rhyo
Normal Spots					
Anorthite -#3	233	4	82.5	1.7	0.45
Anorthite -#4	234	4	84.0	2.1	0.66
Anorthite -#5	214.4	1.4	77.3	1.9	0.54
Anorthite -#6	247.4	1.9	88.4	2.0	0.23
Anorthite -#8	234	3	84.2	2.3	0.57
Anorthite -#9	198	3	71.2	2.2	0.47
Anorthite -#10 (rim of #8-9)	366	18	132.2	6.3	0.85
Irregular Spots					
Anorthite -#2; small holes on BSE	216	10	62.3	6.3	0.46
Anorthite -#7; many micro-cracks	173	4	60.1	2.9	0.42